Simulation study of superheating in evaporating droplets of (TTIP + *p*-xylene) in spray flame synthesis

Babette Kunstmann[a], Irenäus Wlokas[b], Maximilian Kohns[a,*], Hans Hasse[a]

[a] *Laboratory of Engineering Thermodynamics (LTD), RPTU Kaiserslautern, Erwin-Schrödinger-Str. 44, 67663, Kaiserslautern, Germany*
[b] *EMPI, Institute of Energy and Materials Processes – Fluid Dynamics, University of Duisburg-Essen, Carl-Benz-Str. 199 47048, Duisburg, Germany*

Abstract

Spray flame synthesis is an important technique for the production of metal oxide nanoparticles. Micro-explosions of the burning and evaporating droplet are an important breakup mechanism that is usually necessary in order to achieve a homogeneous product quality. There is an ongoing debate on the causes of these micro-explosions. With the present simulation study, we contribute to the clarification of this issue. Simulations of the evaporation of droplets of titanium (IV) isopropoxide (TTIP) dissolved in *p*-xylene, for which detailed information on thermophysical properties is available, are carried out for two scenarios representing single droplet combustion experiments and spray flame combustion, respectively. A one-dimensional model is developed, in which both the energy transport and the mass transport inside the droplet and the corresponding convective boundary conditions are considered. From the temperature and concentration profiles in the droplet, the superheating is calculated, considering the non-ideality of the liquid phase. The results show that superheating sets in inside the droplet. Hence, after reaching a certain threshold, a sudden evaporation will occur inside the droplet — and cause the micro-explosion. This effect is related to large values of the Lewis number, indicating that the heat conduction is much faster than the mass diffusion. As the Lewis number is not only large for the system studied here but also for other precursor solutions used in spray flame synthesis, the explanation of the observed micro-explosions is expected to hold in many cases.

*Corresponding author

1. Introduction

Spray flame synthesis is a versatile process for the production of functional nanomaterials. In this process, a metal-containing precursor is dissolved typically in a combustible solvent. This so-called precursor solution is atomized and ignited to generate a spray flame, in which metal oxide nanoparticles form. The properties of the product particles strongly depend on the evaporation and disintegration process of the precursor solution droplets. [1, 2] Micro-explosions of these droplets have been observed and lead to an improved product quality [3–5]. Several hypotheses for the causes of micro-explosions in spray flame synthesis have been proposed in the literature. Stark et al. [6] suggest that micro-explosions are caused by the rapid heating of the droplets in the flame leading to decarboxylation of carboxylic acid salt precursors. The associated release of gaseous CO_2 is believed to initiate micro-explosions. Rosebrock et al. [7] propose the following mechanism for micro-explosions: the preferential evaporation of the low-boiling solvent leads to an accumulation of higher-boiling precursor components at the droplet surface, which in turn causes a temperature increase there. This favors the thermal decomposition of the precursor into viscous intermediates. The high viscosity and the connected low mass diffusivity in the outer region of the droplet, which is referred to as a "viscous shell", leads to the superheating of the low-boiling solvent in the droplet and, finally, to micro-explosions. The same mechanism is described by Meierhofer et al. [8]. Li et al. [9] attribute micro-explosions to a similar mechanism with shell formation. However, they claim that also solid products from the precursor decomposition reactions contribute to the shell formation, referring to the mechanism described for slurry droplet micro-explosions [10]. Skenderović et al. [11] suggest that micro-explosions are caused by the precipitation of salt precursors at the surface of the droplet, where the precursor concentration is highest. Angel et al. [12] assume that reactions between precursor and solvent components lead to the formation of explosive nitrate esters or metal carboxylates, which can release CO_2 during decarboxylation at high temperatures as also described by Stark et al. [6].

Micro-explosions have been observed in studies of fuel blend droplet evaporation for a long time [13–17]. In this field, the occurrence of the micro-explosions of multicomponent fuel droplets is usually attributed to a superheating inside the droplet, which gives rise to the explosion when vaporization sets in. This occurs only for mixtures and only when the heat conduction is faster than the mass diffusion. Then, the temperature inside the droplet in a hot atmosphere rises faster than the droplet interior is depleted from the low-boiling component that evaporates preferentially. Therefore, the droplet interior can become superheated and, eventually, homogeneous or heterogeneous vapor nucleation can occur. [13–17] The Lewis number Le is used as a measure for the difference between heat conduction and mass diffusion rates. It is defined as:

$$Le = \frac{a}{D}, \tag{1}$$

where a is the liquid thermal diffusivity and D is the Fickian diffusion coefficient in the liquid phase. The thermal diffusivity a can be calculated from the thermal conductivity λ, the density ρ, and the isobaric heat

capacity c_p:

$$a = \frac{\lambda}{\rho c_p} \tag{2}$$

High Lewis numbers indicate slow diffusive mass transport compared to fast heat conduction and, thus, a higher probability for droplet superheating and micro-explosion. [13] While this process is challenging to observe experimentally, it can be described readily using mathematical and numerical models.

Models for droplet heating, evaporation, and combustion have been developed for several decades now, mainly focusing on applications in fuel combustion [18–23]. These models describe the temporal evolution of the properties of a single droplet in a hot atmosphere. There are models in which the droplet is represented with resolution in its radial coordinate while others assume the droplet to be well-mixed and consider only lumped droplet properties. Some of these droplet evaporation and combustion models have also been adapted for investigations of the spray flame synthesis process [4, 11, 24–30]. The models are sometimes designed to be included in more complex simulations on a larger scale, such as computational fluid dynamics (CFD) [24, 25, 27, 28] or Monte-Carlo simulations of combustion [11]. Others aim at gaining a deeper insight into the processes inside the droplet [4, 26, 29].

Li et al. [4] propose a one-dimensional droplet evaporation model based on the work of Law [13] and Zhang and Law [31] to evaluate temperature and concentration profiles for optical diagnostics of single droplet combustion experiments. They study droplets consisting of tin (II) 2-ethylhexanoate and xylene experimentally and numerically. Using the diffusion-limit approach, the liquid phase is spatially resolved and the time-dependence of the thermophysical properties is considered. However, due to the lack of property data for the system, especially for tin (II) 2-ethylhexanoate, the properties of the pure components as well as the mixtures are only estimated.

Ren et al. [26] also base their one-dimensional model on the work of Law [13] and Zhang and Law [31]. They present a comprehensive multicomponent droplet combustion model including the precursor reaction pathways and particle formation routes. Mixtures of 2-ethylhexanoic acid and *m*-xylene with and without the precursor tin (II) 2-ethylhexanoate are studied. Due to the lack of property data, the missing properties of the precursor tin (II) 2-ethylhexanoate are assumed to be similar to those of 2-ethylhexanoic acid. The properties of the pure components are estimated by group contribution methods and mixture properties are calculated assuming ideal mixing behavior. The diffusion coefficients in the liquid phase are used as control parameters. Gas, liquid and solid phases are described in detail. The influence of the liquid phase Lewis number on the temperature and composition profiles and on the occurrence of micro-explosions is considered. The boiling point of the liquid mixture is examined. The micro-explosion time, which the authors define as the time until the mixture boiling point is reached in the droplet interior, is found to decrease with increasing Lewis number. In short: the results from Ren et al. [26] support the hypothesis that the micro-explosions are caused by superheating, and, because of a lack of fluid property data, they carry out parametric studies

related to this phenomenon.

The model presented by Narasu et al. [28] is similar to that from their previous work [27] and based on the works of Abramzon and Sirignano [20] and Brenn et al. [32]. They study the evaporation of droplets consisting of titanium (IV) isopropoxide (TTIP) and *p*-xylene in a hot environment with convective boundary conditions as lumped systems. Their model includes liquid phase properties based on the measurements and correlations by Keller et al. [33]. The model was recently extended and now resolves the liquid interior spatially [29]. This extended one-dimensional model also includes a shell-formation mechanism and thereby considers induced puffing and micro-explosion events.

In the present work, we investigate whether superheating is likely to cause the micro-explosions in spray flame synthesis by simulations of an evaporating droplet of a precursor mixture, for which the thermophysical properties are well-known. The droplet is described by a one-dimensional model in spherical coordinates, accounting for both diffusion and heat conduction in the droplet, alongside with the corresponding convective boundary conditions. From the concentration and temperature profiles, information on the superheating is obtained. The degree of superheating that is needed to induce evaporation is hard to estimate for the extremely high rates of the temperature and concentration changes in the droplets in spray flame synthesis. Furthermore, not only homogeneous but also heterogeneous nucleation might occur [4].

(TTIP + *p*-xylene) is chosen as the precursor solution in this study because a comprehensive set of thermophysical properties is available for this system [33]. Moreover, no liquid phase reactions and no solid precipitation have been observed for this system and the decomposition of the components occurs only at high temperatures above 600 °C. [8, 34] Furthermore, data from single droplet combustion experiments are available, which confirm the occurrence of micro-explosions in this system. [9]

Figure 1 shows the Lewis number Le of (TTIP + *p*-xylene) mixtures as a function of the *p*-xylene mole fraction at different temperatures. The Lewis number Le was calculated using correlations from Ref. [33] and the Fickian diffusion coefficient (cf. section 2.5.1). Le is significantly larger than 40 in all cases. Therefore, the heat conduction is always much faster than the mass diffusion, which makes the occurrence of superheating phenomena during the evaporation of a (TTIP + *p*-xylene) droplet likely.

2. Model

2.1. Overview

The present evaporating droplet model is inspired by the work of Faeth [18]. The droplet is spherical, all processes are radially symmetric, the radial coordinate is r. The pressure is always 1 bar. The droplet consists of two components i = (TTIP, *p*-xylene). Heat conduction and diffusion inside the droplet are described and the mass and energy balance equations are solved considering convective boundary conditions, resulting in the mole fraction profiles $x_i(r,t)$ of both components and the temperature profile $T(r,t)$. The droplet is assumed to be in convective contact with an ambient gas (g) with a constant temperature T_∞ and $y_{\infty,i} = 0$,

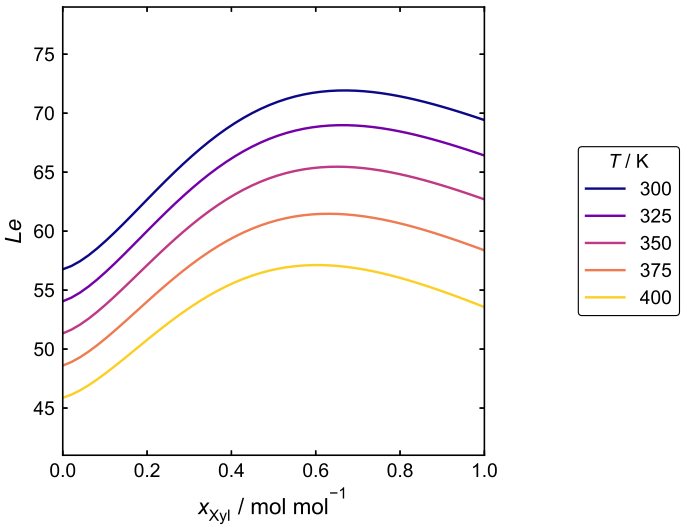

Figure 1: Lewis number of (TTIP + p-xylene) mixtures as a function of the p-xylene mole fraction at different temperatures.

where y_i is the mole fraction of the component i (i = TTIP, p-xylene) in the gas phase. The heat flow into the droplet is $\dot{Q}$, the mass flows of the evaporating components are $\dot{m}_i$ (i = (TTIP, p-xylene)). The solubility of the gas in the liquid is neglected. The liquid phase properties — density ρ, thermal conductivity λ, isobaric heat capacity c_p, and (binary) diffusion coefficient D — depend on the temperature and the composition and, therefore, on the radial coordinate r and the time t. Additionally, the radius R of the droplet varies with time. A sketch of the model is shown in Figure 2.

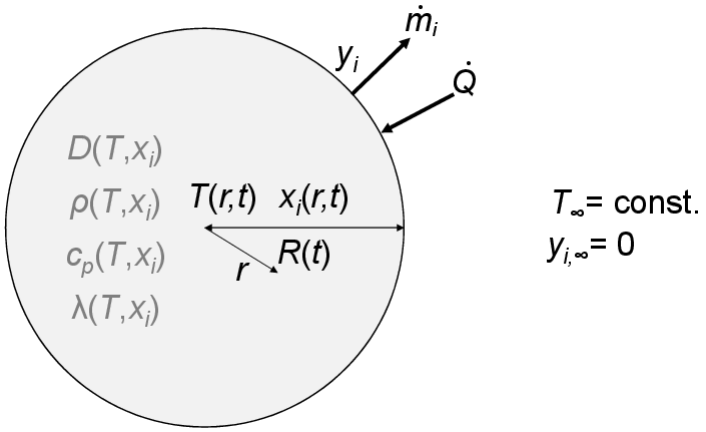

Figure 2: Sketch of the model.

2.2. Governing equations

In this work, the heat transfer in the droplet is described by the one-dimensional transient heat conduction equation in spherical coordinates under consideration of variable fluid properties (see [35]):

$$\frac{\partial T}{\partial t} = \frac{\lambda}{\rho c_p}\left[\frac{\partial^2 T}{\partial r^2} + \left(\frac{2}{r} + \frac{1}{\lambda}\frac{\partial \lambda}{\partial r}\right)\frac{\partial T}{\partial r}\right] - T\left(\frac{1}{\rho}\frac{\partial \rho}{\partial t} + \frac{1}{c_p}\frac{\partial c_p}{\partial t}\right) \tag{3}$$

The fluid is a binary liquid mixture. The mass transfer in the droplet is analogously described by the one-dimensional transient diffusion equation for each of the two liquid phase components i, allowing for variable fluid properties [35]:

$$\frac{\partial x_i^{(m)}}{\partial t} = D\left[\frac{\partial^2 x_i^{(m)}}{\partial r^2} + \left(\frac{2}{r} + \frac{1}{\rho}\frac{\partial \rho}{\partial r} + \frac{1}{D}\frac{\partial D}{\partial r}\right)\frac{\partial x_i^{(m)}}{\partial r}\right] - x_i^{(m)}\frac{1}{\rho}\frac{\partial \rho}{\partial t} \tag{4}$$

Therein, $x_i^{(m)}$ is the mass fraction of component i and D is the binary Fickian diffusion coefficient. In the derivation of eqs. (3) and (4) it is assumed that there is no convection inside the droplet.

2.3. Boundary conditions

In the droplet center at $r = 0$, Neumann boundary conditions are applied:

$$\left.\frac{\partial T}{\partial r}\right|_{r=0} = 0 \tag{5}$$

$$\left.\frac{\partial x_i^{(m)}}{\partial r}\right|_{r=0} = 0 \tag{6}$$

At the outer radius R of the droplet, the coupling of heat and mass transfer during evaporation has to be taken into account. The time derivative of the droplet radius $R(t)$ is calculated by [35]:

$$\frac{\mathrm{d}R}{\mathrm{d}t} = -\frac{1}{\rho(r=R,t)R^2}\left(\frac{\sum \dot{m}_i}{4\pi} + \int_0^R \frac{\partial \rho}{\partial t} r^2 \mathrm{d}r\right) \tag{7}$$

Throughout this work, the $\sum$ sign denotes a summation over the two liquid phase components. The convective boundary conditions used here were taken from Ref. [18] and consider the presence of the gas (that is assumed to be insoluble in the liquid) in addition to the evaporating components. The evaporating mass flow $\dot{m}_i$ of component i is calculated by [18]:

$$\dot{m}_i = 2\pi R \rho_\mathrm{g} D_{i,\mathrm{g}}\, Sh_i\, \varepsilon_i B_\mathrm{M} \tag{8}$$

Therein, ρ_g is the ambient gas density and $D_{i,\mathrm{g}}$ is the diffusion coefficient of component i at infinite dilution in the ambient gas. The calculation of the Sherwood number Sh_i is described in section 2.4. B_M is the Spalding mass transfer number, which is defined as [18]:

$$B_\mathrm{M} = \frac{\sum y_i^{(m)}}{1 - \sum y_i^{(m)}} \tag{9}$$

The partial evaporation rate ε_i is then obtained from:

$$\varepsilon_i = \frac{\dot{m}_i}{\dot{m}} = \frac{y_i^{(m)}(1 + B_\mathrm{M})}{B_\mathrm{M}} \tag{10}$$

$y_i^{(m)}$ is the mass fraction of the evaporating component i in the gas phase at the droplet surface. It is calculated from the corresponding mole fraction y_i using the molar masses of the evaporating components M_i and the ambient gas molar mass M_g:

$$y_i^{(m)} = \frac{y_i M_i}{\sum y_i M_i + (1 - \sum y_i) M_\mathrm{g}} \tag{11}$$

y_i, the mole fraction of component i in the gas phase at the droplet surface, is calculated from the vapor-liquid equilibrium at the droplet surface using the extended Raoult's law:

$$y_i = \frac{[p_i^\mathrm{v}(T) x_i \gamma_i]_{r=R}}{p} \tag{12}$$

Therein, p_i^v is the vapor pressure of the pure component i, x_i is the liquid phase mole fraction of component i, γ_i is the activity coefficient of component i, all of which are evaluated at the outer droplet radius $r = R$, and p is the pressure.

The net heat flow into the droplet at the outer radius is given by [18]:

$$\dot{Q} = 2\pi R \lambda_\mathrm{g}\ Nu\ (T_\infty - T(R)) - \sum \dot{m}_i \Delta h_i^{\mathrm{v},(m)} \tag{13}$$

The calculation of the Nusselt number Nu is described in section 2.4. λ_g is the ambient gas thermal conductivity and $\Delta h_i^{\mathrm{v},(m)}$ is the specific enthalpy of vaporization of the component i.

2.4. Characteristic heat and mass transfer numbers

The characteristic heat and mass transfer numbers are calculated as suggested by Faeth [18]. The characteristic numbers are obtained from empirical correlations and subsequently corrected for convection. The equations for the uncorrected Nusselt number Nu_0 and Sherwood number $Sh_{0,i}$ of component i are:

$$Nu_0 = \left(2 + \frac{0.555\ Re^{1/2} Pr^{1/3}}{\left(1 + \frac{1.232}{Re\ Pr^{4/3}}\right)^{1/2}} \right) \tag{14}$$

$$Sh_{0,i} = \left(2 + \frac{0.555\ Re^{1/2} Sc_i^{1/3}}{\left(1 + \frac{1.232}{Re\ Sc_i^{4/3}}\right)^{1/2}} \right) \tag{15}$$

The Reynolds number Re is given by

$$Re = \frac{u \rho_\mathrm{g} 2R}{\eta_\mathrm{g}} \tag{16}$$

with the droplet velocity u and the viscosity of the ambient gas η_g. The Prandtl number Pr and Schmidt number Sc_i of component i are calculated by:

$$Pr = \frac{\eta_\mathrm{g} c_{p,\mathrm{g}}}{\lambda_\mathrm{g}} \tag{17}$$

$$Sc_i = \frac{\eta_\mathrm{g}}{\rho_\mathrm{g} D_{i,\mathrm{g}}} \tag{18}$$

$c_{p,\mathrm{g}}$ is the isobaric heat capacity of the ambient gas and $D_{i,\mathrm{g}}$ is, again, the diffusion coefficient of component i at infinite dilution in the ambient gas.

These Nusselt and Sherwood numbers are subsequently corrected for convection using the Spalding mass transfer number B_M (see eq. (9)) and the Spalding heat transfer number B_T, which is given by:

$$B_\mathrm{T} = \frac{\bar{c}_{p,\mathrm{v}}(T_\infty - T(R))}{\dot{Q}/\dot{m}} \tag{19}$$

Therein, $\bar{c}_{p,\mathrm{v}} = \sum \varepsilon_i c_{p,\mathrm{v},i}$ is the mass flux-weighted average heat capacity of the evaporating species in the vapor phase. The equations for the Nusselt and Sherwood numbers with convection correction are:

$$Nu = Nu_0 \, \frac{\ln(1 + B_\mathrm{T})}{B_\mathrm{T}} \tag{20}$$

$$Sh_i = Sh_{0,i} \, \frac{\ln(1 + B_\mathrm{M})}{B_\mathrm{M}} \tag{21}$$

2.5. Property models

2.5.1. Liquid phase

In this work, the liquid phase is a binary mixture of TTIP and *p*-xylene. The density, thermal conductivity, isobaric heat capacity, and self-diffusion coefficients in liquid mixtures of TTIP and *p*-xylene were calculated from the correlations provided by Keller et al. [33]. The enthalpy of vaporization was calculated using the Clausius-Clapeyron equation and from the vapor pressure curves given in Ref. [33]. The activity coefficients for vapor-liquid equilibrium calculations were evaluated from the non-random two liquid (NRTL) model with parameters taken from Keller et al. [33]. The binary Maxwell-Stefan mutual diffusion coefficient $Đ$ was obtained from the self-diffusion coefficients at infinite dilution $Đ_{12}^\infty$ and $Đ_{21}^\infty$ using the Vignes correlation:

$$Đ = (Đ_{12}^\infty)^{x_1} (Đ_{21}^\infty)^{x_2} \tag{22}$$

The Fickian mutual diffusion coefficient D, which is used in the mass transport equation (eq. (4)), was finally calculated from the Maxwell-Stefan diffusion coefficient and the thermodynamic factor Γ:

$$D = Đ\Gamma, \tag{23}$$

where Γ is

$$\Gamma = 1 + x_1 \frac{\partial \ln \gamma_1}{\partial x_1} = 1 + x_2 \frac{\partial \ln \gamma_2}{\partial x_2} \tag{24}$$

in a binary system.

2.5.2. Gas phase

The gas phase in the model consists of pure oxygen. The gas phase properties of oxygen were calculated as follows. The density ρ_g was obtained from the ideal gas law. The viscosity η_g was calculated using Lucas's method [36]. The thermal conductivity λ_g and the isobaric heat capacity $c_{p,\mathrm{g}}$ were calculated using correlations and parameters from Ref. [37]. The diffusion coefficients $D_{i,\mathrm{g}}$ of TTIP and *p*-xylene in oxygen were estimated by Fuller's method [36]. The isobaric heat capacities of TTIP and *p*-xylene in the vapor phase $c_{p,\mathrm{v},i}$, which are only needed in eq. (19), were calculated using NASA polynomials [38] with parameters taken from Refs. [39] and [40].

2.6. Implementation

For the solution of the model equations, an explicit finite-difference scheme with forward differences in time with adaptive step size and second-order central differences in space was applied. To ensure the numerical stability of the finite-difference scheme, the following criterion was applied to calculate the time increment Δt for every iteration:

$$\Delta t = 0.1 \min\left(\frac{(\Delta r)^2}{\max(a)}, \frac{(\Delta r)^2}{\max(D)}\right) \tag{25}$$

Therein, Δr is the spatial grid size calculated from the current droplet radius R and the number of spatial grid points. The liquid thermal diffusivity $a = \frac{\lambda}{\rho c_p}$ and the liquid diffusion coefficient D were evaluated at each spatial grid point and the maximum value was used for the calculation of the time increment. The model was set up with 100 spatial nodes and the calculation was terminated when the droplet radius reached 4 µm. The evaporating droplet model and the property models were implemented in *python* using the modules *numpy*, *pandas*, and *scipy*.

3. Results and discussion

3.1. Studied scenarios

Two types of evaporation scenarios with different initial and boundary conditions of the model were considered. The input parameters differing between the two scenarios are the initial droplet diameter d_0, the initial droplet composition $x_{\mathrm{TTIP},0}$ (which was assumed to be uniform), the droplet velocity u, and the ambient temperature T_∞. The latter two were constant during each simulation.

First, these initial and boundary conditions were chosen to emulate the conditions of single droplet combustion experiments. Experimental results for single droplet combustion of droplets containing TTIP and a xylene isomer mixture were reported by Li et al. [9]. In their experimental setup, the ambient temperature is unknown, but is most likely room temperature and the droplets are heated by the spherical flame surrounding them. Combustion processes are not included in the model presented in this work. Therefore, we considered different ambient temperatures for the emulation of this case, ranging from 1000 to 2750 K.

Second, the initial and boundary conditions were set to represent the conditions during flame spray combustion. In this case, the initial droplet sizes are smaller and the droplet velocity is much higher than for the single droplet combustion experiments. Despite the fact that in reality, the droplet velocity and the local temperature of the ambient gas phase vary along the droplet's trajectory [41], this was neglected and constant boundary conditions were used. The initial droplet size, the droplet velocity, and the ambient temperature were set to typical average values for the spray flame combustion process [25, 41–43]. The initial composition was varied within the range reported in the literature for (TTIP + xylene) precursor solutions [8, 44–46].

In all simulation scenarios studied in this work, the (uniform) initial droplet temperature was 300 K. An overview of the initial and boundary conditions of the simulations is given in Table 1.

Table 1: Initial and boundary conditions applied in the simulations.

Case		d_0 / µm	$x_{\mathrm{TTIP},0}$ / mol mol^{-1}	u / m s^{-1}	T_∞ / K
Single droplet combustion	Ia	86	0	0.5	1000 – 2750
	Ib	91	0.07[a]		
Spray flame combustion	II	20	0.01 – 0.3	50	2000

[a] corresponding to an initial TTIP concentration of 0.5 mol L^{-1}

3.2. Results for the droplet diameter

The results for the droplet diameter as a function of time are discussed first. The time span between the start of the simulation and its termination, which is reached when the droplet radius has decreased to 4 µm, is referred to as droplet lifetime in this work.

Figure 3 shows the experimental results from single droplet combustion experiments by Li et al. [9] and simulation results of the present work that were obtained for initial and boundary conditions that were similar, although not the same, as in the corresponding experiment (cf. Table 1, cases Ia and Ib). The normalized squared droplet diameter $(d/d_0)^2$ is shown as a function of the normalized time t/d_0^2, which has been shown to allow for a straightforward comparison of droplets with different initial sizes [19, 28]. As expected, the evaporation process is slower at lower ambient temperatures. The general course of the curves in Figure 3 is similar. For most of the droplet lifetime, the decrease of the droplet size follows the well-known d^2-law [19]. This is in agreement with the experimental results. However, the simulation underestimates the evaporation rate, even for the highest studied temperature. This could be caused by an underestimation of the heat and mass transfer rates between the droplet and the gas phase (i.e., by the boundary conditions), but there are also other possible reasons, such as the simplified mass transfer model inside the droplet. Nevertheless, the model is confirmed qualitatively by the comparison with the experimental data. We have refrained from trying to obtain a quantitative description of this single experiment, which would have required a reparameterization of the model.

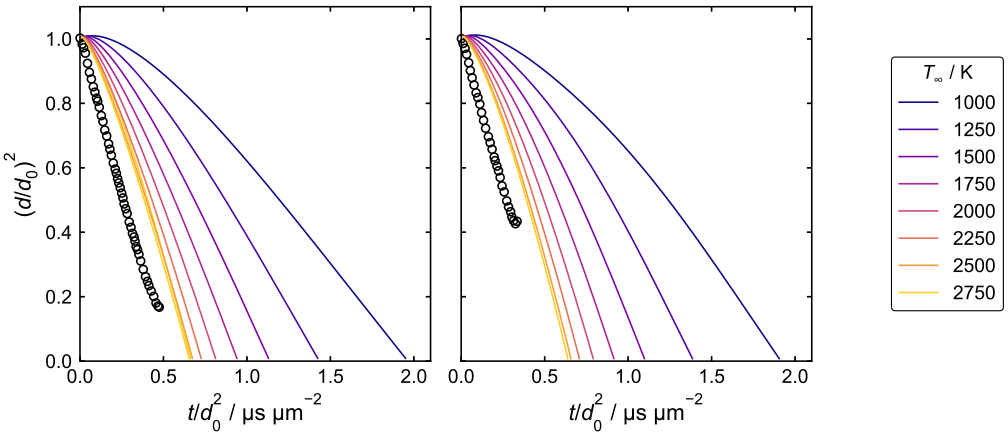

Figure 3: Normalized squared droplet diameters as a function of the normalized time for pure p-xylene (left, case Ia cf. Table 1) and 0.5 M TTIP (≈ 0.07 mol mol^{-1}) in p-xylene (right, case Ib cf. Table 1). Symbols: experimental results [9]. Lines: simulation results.

Figure 4 presents the simulation results for the second type of initial and boundary conditions (case II) essentially in the same way as in Figure 3. However, no experimental data are available for comparison. Results are shown for different initial TTIP mole fractions $x_{\mathrm{TTIP},0}$; the ambient gas temperature is always 2000 K. The shape of the curves is similar as in Figure 3. The droplet lifetime increases slightly with increasing initial TTIP mole fraction, but the overall influence of the initial composition is small. Owing to the scaling of the droplet lifetime with the droplet radius, the normalized droplet lifetime is almost the same as the corresponding previous result at the same temperature from Figure 3, even though the droplet velocity is much higher in case II.

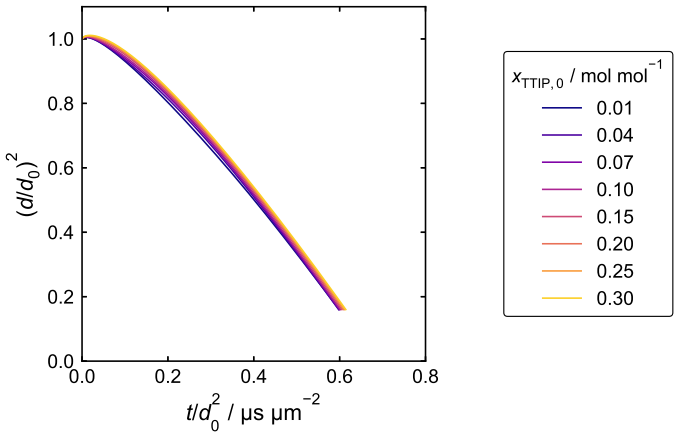

Figure 4: Simulation results for case II from Table 1: normalized squared droplet diameters as a function of the normalized time.

3.3. Results for temperature, composition, and superheating

The spatially resolved temperature and composition profiles in the droplet obtained from the simulation allow to investigate if the liquid is superheated at any position inside the droplet. For this purpose, the vapor pressure of the liquid at the given temperature and composition was compared to the total pressure p. As the pressure difference between the droplet and its surroundings due to the droplet curvature is small for droplet sizes in the micrometer range as they are studied here, the total pressure was always set to 1 bar. Due to the lack of sufficient data for the surface tension of mixtures of TTIP and p-xylene, the detailed quantification of this effect is not possible, which is why the simulations were terminated at $R = 4$ µm as described above, where the influence of the droplet curvature on the internal pressure is still negligible. For characterizing the superheating, we define the so-called superheating index S as follows:

$$S = \sum p_i^{\mathrm{v}}(T) x_i \gamma_i / p \tag{26}$$

For $S > 1$, the liquid is superheated and boiling may set in. The superheating index is calculated using the local temperature and composition at each spatial grid point for each time step. Therefore, the profiles of the superheating index shown in this subsection are an immediate implication of the corresponding temperature and composition profiles.

Figures 5 and 6 show the results for temperature, composition, and superheating index for cases Ia and Ib (cf. Table 1) for an ambient temperature of 2000 K. Figure 5 shows results for the evaporation of a pure p-xylene droplet. As expected, the droplet temperature increases most rapidly at the surface and approaches the boiling temperature of p-xylene at 1 bar (412 K [4, 33]). The temperature in the center of the droplet increases more slowly. For pure components, the vapor pressure depends only on the temperature, so that the superheating index S is directly related to the temperature. Unsurprisingly, the maximum of the superheating index S, which is located at the droplet surface, never exceeds 1 during the entire studied evaporation process.

Figure 6 shows the results for an evaporating (TTIP + p-xylene) droplet (case Ib). The temperature profiles are similar to those observed for the pure p-xylene droplet (cf. Figure 5) at first, but towards the end of the droplet lifetime, a temperature gradient close to the droplet surface remains, whereas the temperature of the pure p-xylene droplet becomes uniform eventually. The mole fraction of the low-boiling component p-xylene decreases strongly at the surface, while the composition in the center of the droplet remains basically unchanged throughout the entire droplet lifetime, due to the slow diffusive mass transfer in the liquid phase. The difference between the shapes of temperature and composition profiles is a consequence of the high Lewis numbers in the liquid phase (cf. Figure 1). The comparatively high thermal diffusivity leads to significant heat conduction to the droplet center. In contrast, the mass diffusion is slow, which leads to the depletion of the low-boiling p-xylene at the surface over time. As a result of the interplay of the temperature and the composition profiles, maxima appear in the profiles of the superheating index. These

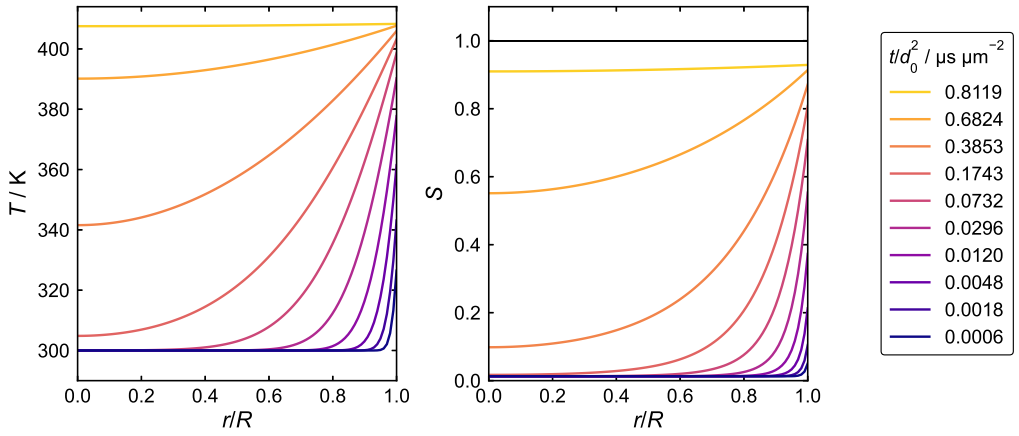

Figure 5: Simulation results for case Ia from Table 1 (pure *p*-xylene): temperature (left) and superheating index (right) in the droplet interior as a function of the dimensionless droplet radius at different normalized times. The ambient temperature is $T_\infty = 2000\,\mathrm{K}$.

maxima are located close to the droplet surface at all times during the evaporation process and can exceed $S = 1$ from a certain time onward.

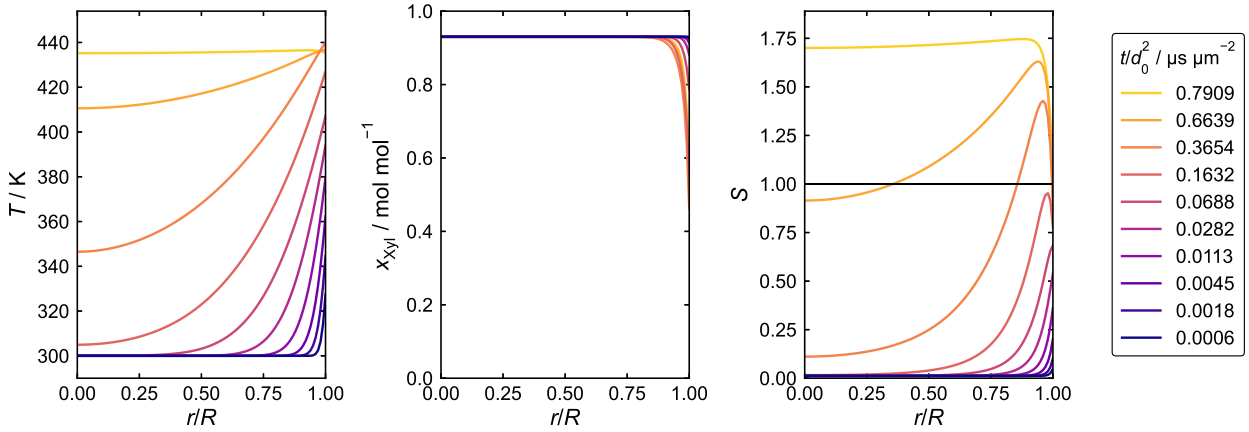

Figure 6: Simulation results for case Ib from Table 1: temperature (left), *p*-xylene mole fraction (center), and superheating index (right) in the droplet interior as a function of the dimensionless droplet radius at different normalized times. The ambient temperature is $T_\infty = 2000\,\mathrm{K}$.

Figure 7 shows the temperature, composition, and superheating index profiles for the evaporation of a (TTIP + *p*-xylene) droplet under initial and boundary conditions representing the spray flame case (case II, cf. Table 1). The initial TTIP mole fraction is $x_{\mathrm{TTIP},0} = 0.07$ mol mol^{-1}. The profiles are almost similar to those in Figure 6. Again, the temperature rises more quickly at the surface than in the center of the droplet, the composition only changes close to the surface, and, therefore, the formation of a pronounced maximum of the superheating index S is observed, which also reaches values above 1 in the droplet lifetime. This indicates that superheating can occur at the conditions in spray flame synthesis.

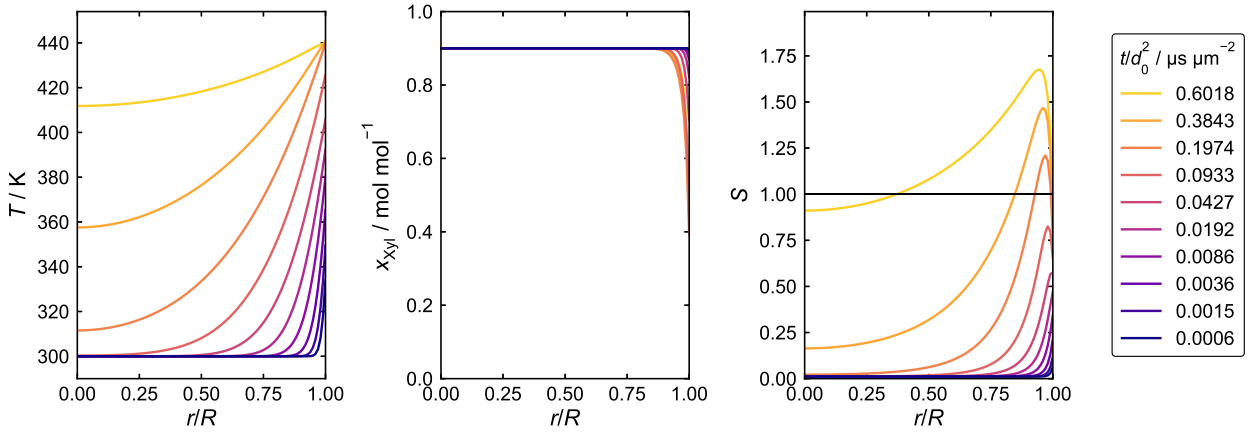

Figure 7: Simulation results for case II from Table 1: temperature (left), p-xylene mole fraction (center), and superheating index (right) in the droplet interior as a function of the dimensionless droplet radius at different normalized times. The initial TTIP mole fraction is $x_{\mathrm{TTIP},0} = 0.07$ mol mol^{-1}.

3.4. Results for the superheating maxima

In this subsection, the results for the superheating index are discussed in more detail. Vaporization can in principle set in anytime at any position where $S > 1$. In practice, however, a certain threshold in S must be exceeded for bubble nucleation to set in. The spinodal gives an upper limit of S, above which nucleation will occur instantaneously, but it must be expected that nucleation sets in well before that limit is reached. The exact point of the onset of nucleation is difficult to predict, as it depends on many parameters, such as the rate at which S changes and the purity of the mixture. Therefore, different values of the superheating index are considered ($S^* \geq 1$, 1.4, 1.6, 1.8). For all simulations of evaporating mixture droplets (cf. Table 1, cases Ib and II), the time and dimensionless droplet radius for which these thresholds of the superheating index S^* are reached for the first time were determined.

The position at which vapor nucleation occurs is important for the micro-explosion event. Two basic modes of the micro-explosions have been described in the literature [3, 4, 43, 47]: in the first mode, which is sometimes called puffing, a fog-like swarm of small droplets is ejected from the droplet at a certain position, but otherwise the parent droplet remains largely intact. The change of momentum upon the ejection leads to an abrupt change in the flight direction of the parent droplet. In the second mode, the parent droplet is torn apart and dispersed into a large number of smaller droplets flying in different directions. These modes can be associated with the position in the droplet, where the sudden evaporation sets in: the first mode (puffing) is expected, when the evaporation occurs close to the droplet's surface, whereas the second mode is expected when the evaporation sets in deeper in the droplet.

Figure 8 shows the results for the "single droplet combustion" (case Ib, cf. Table 1) for different ambient temperatures. As expected, the superheating index threshold is reached more quickly when the ambient

temperature increases and it takes longer to reach higher thresholds (cf. left panel in Figure 8). $S^* \geq 1.8$ is reached only for ambient temperatures below 2000 K, likely due to the longer droplet lifetimes at lower temperatures. The position at which a given superheating index is reached first (cf. right panel of Figure 8) depends both on the ambient temperature T_∞ and the value of S^*. For low T_∞, the position moves inside the droplet, and the same holds for larger values of S^*. However, in most studied cases the onset of vaporization occurs rather close to the droplet surface ($r/R > 0.8$), which indicates a preference for puffing. This is in agreement with results by Li et al. [47], who observe surface micro-explosions in single droplet combustion experiments with the precursor solution tin (II) 2-ethylhexanoate in xylene, where the outer layer of a droplet is ejected while the inner part of the droplet continues to evaporate and combust. Also, high-speed camera images of exploding droplets of (TTIP + xylene) from Ref. [9] indicate puffing, see supporting information of Ref. [9].

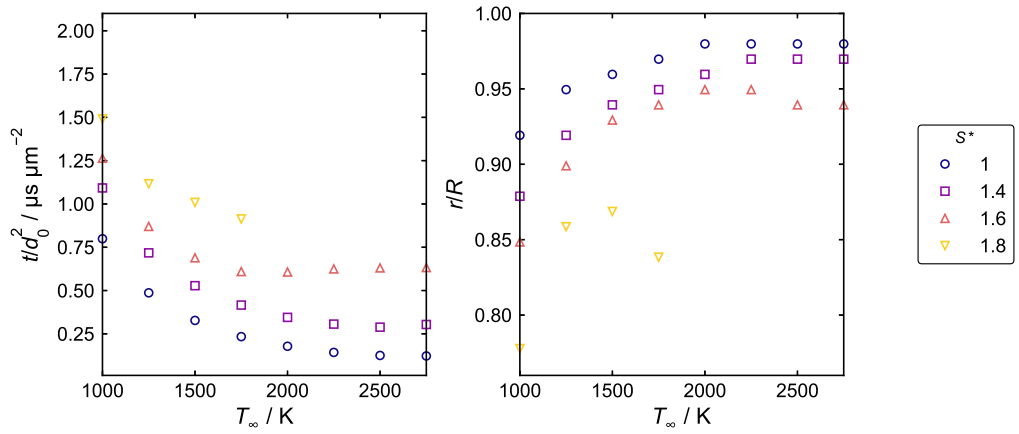

Figure 8: Simulation results for case Ib from Table 1: normalized time (left) and dimensionless droplet radius (right) at which the superheating index first reaches the thresholds indicated in the legend as a function of the ambient temperature. The open symbols show results of individual simulation runs.

Figure 9 shows the corresponding results for the "spray flame combustion" (case II, cf. Table 1) for different initial TTIP mole fractions. The time needed until the threshold is reached (cf. left panel in Figure 9) decreases with increasing initial TTIP mole fraction, in agreement with observations from single droplet combustion experiments, where higher precursor concentrations lead to an earlier onset of micro-explosions [9]. At higher initial TTIP concentrations, the influence of the composition on the time of the onset of vaporization is weaker, even a shallow minimum is observed.

Only the lowest threshold is reached within the droplet lifetime for the lowest initial TTIP mole fraction $x_{\mathrm{TTIP},0} = 0.01$ mol mol^{-1}. Additionally, the values $S^* = 1.4$, $S^* = 1.6$, and $S^* = 1.8$ are also not reached for $x_{\mathrm{TTIP},0} < 0.07$ mol mol^{-1}, $x_{\mathrm{TTIP},0} < 0.1$ mol mol^{-1}, and $x_{\mathrm{TTIP},0} < 0.15$ mol mol^{-1}, respectively. These findings suggest that the occurrence of micro-explosions requires a certain minimum precursor concentration, which is in accord with practical experience.

The position where the threshold is reached (cf. right panel in Figure 9) generally depends only weakly on the initial TTIP mole fraction for a given S^*. The radial positions where the thresholds are reached tend to move slightly towards the droplet interior for higher thresholds. However, in all simulations the positions where S^* is reached first is at $r/R > 0.9$, i.e., near to the droplet surface, indicating a tendency for puffing micro-explosions.

It is not trivial to understand the details of the influence of $x_{\mathrm{TTIP},0}$ on the results presented in Figure 9, but it is clear, that the influence is important, as higher thresholds require higher initial TTIP mole fractions. Superheating also occurs earlier for higher initial TTIP mole fractions. If superheating occurs only close to the end of the droplet lifetime, the influence of the possibly resulting micro-explosion event on the particle synthesis process is likely less important than if the micro-explosion occurs while the droplet is still large. [48] Therefore, a certain minimum initial TTIP content is probably necessary to (a) achieve the necessary level of superheating for a micro-explosion to occur and (b) lead to micro-explosions early enough to have a significant impact on the mass transfer of the precursor from the liquid droplets to the gas phase.

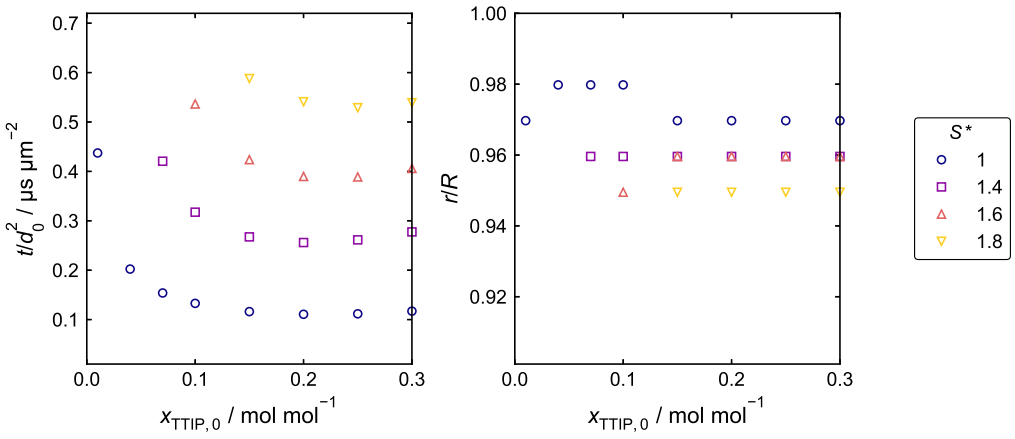

Figure 9: Simulation results for case II from Table 1: normalized time (left) and dimensionless droplet radius (right) at which the superheating index first reaches the thresholds indicated in the legend as a function of the initial TTIP mole fraction. The open symbols show results of individual simulation runs.

4. Conclusions

The introductory mentioned versatility of spray flame synthesis also complicates process design since it offers many degrees of freedom, such as the nature of the precursor and the solvent as well as their concentrations. Moreover, it is known that phenomena such as droplet micro-explosions are key to a homogeneous product quality, but even the reason for their occurrence is still debated. Simulations can provide both a deeper understanding of the reasons of the micro-explosions and, more generally, a means for design and optimization of spray flame synthesis processes.

In this work, we have developed a simple one-dimensional model of an evaporating single droplet that is suited for conceptual studies of spray flame processes, namely on investigating the reasons of the micro-explosions and the influence of process parameters such as the precursor solution properties on their occurrence.

With the model, we were able to provide an explanation for the droplet micro-explosions: the fact that the heat conduction is much faster than the diffusion in typical precursor solutions leads to the occurrence of superheating inside the droplet, which can eventually lead to the nucleation of a vapor bubble inside the droplet and thereby induce a micro-explosion. In a study with mixtures of (TTIP + *p*-xylene), which we have carried out based on detailed information on the fluid properties, such superheated states were observed mostly in the vicinity of the droplet surface, suggesting that so-called surface micro-explosions or puffing events are dominant in the system (TTIP + *p*-xylene), which is in agreement with experimental observations from the literature.

The new model can, hence, be used as a tool to investigate if micro-explosions are to be expected in a precursor system if suitable information on the needed fluid properties is available. This allows to identify promising precursor solutions and to optimize their composition with respect to the occurrence of micro-explosions. In addition, due to its simplicity, the model could also be integrated into more complex simulation scenarios, such as CFD calculations, for improving spray flame synthesis processes.

5. Acknowledgment

This work was supported by the German Research Foundation (DFG) within the priority program SPP 1980 SPRAYSYN under the grants HA 1993/18-2 and KO 5844/2-2.

References

[1] W. Y. Teoh, R. Amal, L. Mädler, Flame spray pyrolysis: An enabling technology for nanoparticles design and fabrication, Nanoscale 2 (2010) 1324. URL: http://xlink.rsc.org/?DOI=c0nr00017e. doi:10.1039/c0nr00017e.

[2] F. Meierhofer, U. Fritsching, Synthesis of metal oxide nanoparticles in flame sprays: Review on process technology, modeling, and diagnostics, Energy and Fuels 35 (2021) 5495–5537. URL: https://pubs.acs.org/doi/10.1021/acs.energyfuels.0c04054. doi:10.1021/acs.energyfuels.0c04054.

[3] C. D. Rosebrock, T. Wriedt, L. Mädler, K. Wegner, The role of microexplosions in flame spray synthesis for homogeneous nanopowders from low-cost metal precursors, AIChE Journal 62 (2016) 381–391. URL: https://onlinelibrary.wiley.com/doi/10.1002/aic.15056. doi:10.1002/aic.15056.

[4] H. Li, C. D. Rosebrock, Y. Wu, T. Wriedt, L. Mädler, Single droplet combustion of precursor/solvent solutions for nanoparticle production: Optical diagnostics on single isolated burning droplets with micro-explosions, Proceedings of the Combustion Institute 37 (2019) 1203–1211. URL: https://linkinghub.elsevier.com/retrieve/pii/S154074891830316X. doi:10.1016/j.proci.2018.06.133.

[5] C. Liu, S. Pokhrel, C. Tessarek, H. Li, M. Schowalter, A. Rosenauer, M. Eickhoff, S. Li, L. Mädler, Rare-Earth-Doped $Y_4Al_2O_9$ Nanoparticles for Stable Light-Converting Phosphors, ACS Applied Nano Materials 3 (2020) 699–710. URL: https://pubs.acs.org/doi/10.1021/acsanm.9b02231. doi:10.1021/acsanm.9b02231.

[6] W. J. Stark, L. Mädler, M. Maciejewski, S. E. Pratsinis, A. Baiker, Flame synthesis of nanocrystalline ceria-zirconia: Effect of carrier liquid, Chemical Communications 3 (2003) 588–589. doi:10.1039/b211831a.

[7] C. D. Rosebrock, N. Riefler, T. Wriedt, L. Mädler, S. D. Tse, Disruptive burning of precursor/solvent droplets in flame-spray synthesis of nanoparticles, AIChE Journal 59 (2013) 4553–4566. URL: http://doi.wiley.com/10.1002/aic.14234. doi:10.1002/aic.14234.

[8] F. Meierhofer, H. Li, M. Gockeln, R. Kun, T. Grieb, A. Rosenauer, U. Fritsching, J. Kiefer, J. Birkenstock, L. Mädler, S. Pokhrel, Screening precursor-solvent combinations for $Li_4Ti_5O_{12}$ energy storage material using flame spray pyrolysis, ACS Applied Materials and Interfaces 9 (2017) 37760–37777. URL: www.acsami.orghttps://pubs.acs.org/doi/10.1021/acsami.7b11435. doi:10.1021/acsami.7b11435.

[9] H. Li, C. D. Rosebrock, N. Riefler, T. Wriedt, L. Mädler, Experimental investigation on microexplosion of single isolated burning droplets containing titanium tetraisopropoxide for nanoparticle production, Proceedings of the Combustion Institute 36 (2017) 1011–1018. URL: https://linkinghub.elsevier.com/retrieve/pii/S1540748916304953. doi:10.1016/j.proci.2016.09.017.

[10] F. Takahashi, I. J. Heilweil, F. L. Dryer, Disruptive Burning Mechanism of Free Slurry Droplets, Combustion Science and Technology 65 (1989) 151–165. doi:10.1080/00102208908924046.

[11] I. Skenderović, G. Kotalczyk, F. Kruis, Dual Population Balance Monte Carlo Simulation of Particle Synthesis by Flame Spray Pyrolysis, Processes 6 (2018) 253. URL: http://www.mdpi.com/2227-9717/6/12/253. doi:10.3390/pr6120253.

[12] S. Angel, J. Neises, M. Dreyer, K. Friedel Ortega, M. Behrens, Y. Wang, H. Arandiyan, C. Schulz, H. Wiggers, Spray-flame synthesis of La(Fe, Co)O_3 nano-perovskites from metal nitrates, AIChE Journal 66 (2020). URL: https://onlinelibrary.wiley.com/doi/abs/10.1002/aic.16748https://onlinelibrary.wiley.com/doi/10.1002/aic.16748. doi:10.1002/aic.16748.

[13] C. K. Law, Internal boiling and superheating in vaporizing multicomponent droplets, AIChE Journal 24 (1978) 626–632. URL: https://onlinelibrary.wiley.com/doi/10.1002/aic.690240410. doi:10.1002/aic.690240410.

[14] J. C. Lasheras, A. C. Fernandez-Pello, F. L. Dryer, Experimental Observations on the Disruptive Combustion of Free Droplets of Multicomponent Fuels, Combustion Science and Technology 22 (1980) 195–209. URL: http://www.tandfonline.com/doi/abs/10.1080/00102208008952383. doi:10.1080/00102208008952383.

[15] S. K. Aggarwal, Modeling of a dilute vaporizing multicomponent fuel spray, International Journal of Heat and Mass Transfer 30 (1987) 1949–1961. URL: https://linkinghub.elsevier.com/retrieve/pii/0017931087902535. doi:10.1016/0017-9310(87)90253-5.

[16] M. Botero, Y. Huang, D. Zhu, A. Molina, C. Law, Synergistic combustion of droplets of ethanol, diesel and biodiesel mixtures, Fuel 94 (2012) 342–347. URL: https://linkinghub.elsevier.com/retrieve/pii/S0016236111006673. doi:10.1016/j.fuel.2011.10.049.

[17] A. Hoxie, R. Schoo, J. Braden, Microexplosive combustion behavior of blended soybean oil and butanol droplets, Fuel 120 (2014) 22–29. URL: https://linkinghub.elsevier.com/retrieve/pii/S0016236113011071. doi:10.1016/j.fuel.2013.11.036.

[18] G. Faeth, Current status of droplet and liquid combustion, Progress in Energy and Combustion Science 3 (1977) 191–224. URL: https://linkinghub.elsevier.com/retrieve/pii/0360128577900120. doi:10.1016/0360-1285(77)90012-0.

[19] W. A. Sirignano, Fuel droplet vaporization and spray combustion theory, Progress in Energy and Combustion Science 9 (1983) 291–322. URL: https://linkinghub.elsevier.com/retrieve/pii/0360128583900114. doi:10.1016/0360-1285(83)90011-4.

[20] B. Abramzon, W. Sirignano, Droplet vaporization model for spray combustion calculations, International Journal of Heat and Mass Transfer 32 (1989) 1605–1618. URL: https://linkinghub.elsevier.com/retrieve/pii/0017931089900434. doi:10.1016/0017-9310(89)90043-4.

[21] J. Tamim, W. Hallett, A continuous thermodynamics model for multicomponent droplet vaporization, Chemical Engineering Science 50 (1995) 2933–2942. URL: https://linkinghub.elsevier.com/retrieve/pii/000925099500131N. doi:10.1016/0009-2509(95)00131-N.

[22] S. S. Sazhin, Advanced models of fuel droplet heating and evaporation, Progress in Energy and Combustion Science 32

(2006) 162–214. URL: https://linkinghub.elsevier.com/retrieve/pii/S0360128505000535. doi:10.1016/j.pecs.2005.11.001.

[23] S. S. Sazhin, Modelling of fuel droplet heating and evaporation: Recent results and unsolved problems, Fuel 196 (2017) 69–101. URL: https://linkinghub.elsevier.com/retrieve/pii/S0016236117300583. doi:10.1016/j.fuel.2017.01.048.

[24] M. C. Heine, S. E. Pratsinis, Droplet and particle dynamics during flame spray synthesis of nanoparticles, Industrial and Engineering Chemistry Research 44 (2005) 6222–6232. URL: https://pubs.acs.org/doi/10.1021/ie0490278. doi:10.1021/ie0490278.

[25] A. J. Gröhn, S. E. Pratsinis, K. Wegner, Fluid-particle dynamics during combustion spray aerosol synthesis of ZrO_2, Chemical Engineering Journal 191 (2012) 491–502. URL: https://linkinghub.elsevier.com/retrieve/pii/S1385894712003269. doi:10.1016/j.cej.2012.02.093.

[26] Y. Ren, J. Cai, H. Pitsch, Theoretical single-droplet model for particle formation in flame spray pyrolysis, Energy and Fuels 35 (2021) 1750–1759. URL: https://dx.doi.org/10.1021/acs.energyfuels.0c03669https://pubs.acs.org/doi/10.1021/acs.energyfuels.0c03669. doi:10.1021/acs.energyfuels.0c03669. arXiv:2002.11535.

[27] P. Narasu, A. Keller, M. Kohns, H. Hasse, E. Gutheil, Numerical study of the evaporation and thermal decomposition of a single iron(III) nitrate nonahydrate/ethanol droplet, International Journal of Thermal Sciences 170 (2021) 107133. URL: https://linkinghub.elsevier.com/retrieve/pii/S1290072921002957. doi:10.1016/j.ijthermalsci.2021.107133.

[28] P. Narasu, M. Nanjaiah, I. Wlokas, E. Gutheil, Numerical simulation and parameterization of the heating and evaporation of a titanium (IV) isopropoxide/p-xylene precursor/solvent droplet in hot convective air, International Journal of Multiphase Flow 150 (2022) 104006. URL: https://linkinghub.elsevier.com/retrieve/pii/S0301932222000283. doi:10.1016/j.ijmultiphaseflow.2022.104006.

[29] P. Narasu, E. Gutheil, A new model for puffing and micro-explosion of single titanium(IV) isopropoxide/p-xylene precursor solution droplets, International Journal of Heat and Mass Transfer 202 (2023) 123647. URL: https://linkinghub.elsevier.com/retrieve/pii/S0017931022011164. doi:10.1016/j.ijheatmasstransfer.2022.123647.

[30] M. Najimu, V. Baghdassarian, S. Leask, V. McDonell, B. Padak, E. Sasmaz, Incorporation of film theory in single droplet combustion model for prediction of precursor release in flame spray pyrolysis, Proceedings of the Combustion Institute 000 (2023) 1–11. URL: https://linkinghub.elsevier.com/retrieve/pii/S1540748923000020. doi:10.1016/j.proci.2022.12.001.

[31] H. Q. Zhang, C. K. Law, Effects of temporally varying liquid-phase mass diffusivity in multicomponent droplet gasification, Combustion and Flame 153 (2008) 593–602. URL: https://linkinghub.elsevier.com/retrieve/pii/S0010218008000242. doi:10.1016/j.combustflame.2007.12.007.

[32] G. Brenn, L. J. Deviprasath, F. Durst, C. Fink, Evaporation of acoustically levitated multi-component liquid droplets, International Journal of Heat and Mass Transfer 50 (2007) 5073–5086. URL: https://linkinghub.elsevier.com/retrieve/pii/S0017931007004917. doi:10.1016/j.ijheatmasstransfer.2007.07.036.

[33] A. Keller, I. Wlokas, M. Kohns, H. Hasse, Thermophysical properties of mixtures of titanium(IV) isopropoxide (TTIP) and p-xylene, Journal of Chemical and Engineering Data 65 (2020) 869–876. URL: https://pubs.acs.org/doi/10.1021/acs.jced.9b01059. doi:10.1021/acs.jced.9b01059.

[34] M. Gonchikzhapov, T. Kasper, Decomposition reactions of $Fe(CO)_5$, $Fe(C_5H_5)_2$, and TTIP as precursors for the spray-flame synthesis of nanoparticles in partial spray evaporation at low temperatures, Industrial and Engineering Chemistry Research 59 (2020) 8551–8561. URL: https://pubs.acs.org/doi/10.1021/acs.iecr.9b06667. doi:10.1021/acs.iecr.9b06667.

[35] R. Kneer, M. Schneider, B. Noll, S. Wittig, Diffusion controlled evaporation of a multicomponent droplet: theoretical studies on the importance of variable liquid properties, International Journal of Heat and Mass Transfer 36 (1993) 2403–2415. URL: https://linkinghub.elsevier.com/retrieve/pii/S0017931005801243. doi:10.1016/S0017-9310(05)80124-3.

[36] B. E. Poling, J. M. Prausnitz, J. P. O'Connell, The properties of gases and liquids, Chemical engineering, McGraw-Hill, 2001. doi:10.1036/0070116822.

[37] VDI (Ed.), VDI-Wärmeatlas, Springer Berlin Heidelberg, Berlin, Heidelberg, 2013. URL: http://link.springer.com/10.1007/978-3-642-19981-3. doi:10.1007/978-3-642-19981-3.

[38] F. J. Zeleznik, A General IBM 704 Or 7090 Computer Program for Computation of Chemical Equilibrium Compositions, Rocket Performance, and Chapman-Jouguet Dentonations: Frank J. Zeleznik and Sanford Gordon, National Aeronautics and Space Administration, 1962.

[39] P. Buerger, D. Nurkowski, J. Akroyd, M. Kraft, A kinetic mechanism for the thermal decomposition of titanium tetraisopropoxide, Proceedings of the Combustion Institute 36 (2017) 1019–1027. URL: https://linkinghub.elsevier.com/retrieve/pii/S1540748916304515. doi:10.1016/j.proci.2016.08.062.

[40] J. A. Draeger, D. W. Scott, Ideal gas thermodynamic properties of 1,4-dimethylbenzene, The Journal of Chemical Physics 74 (1981) 4748–4749. URL: http://aip.scitation.org/doi/10.1063/1.441629. doi:10.1063/1.441629.

[41] F. J. Martins, J. Kirchmann, A. Kronenburg, F. Beyrau, Experimental investigation of axisymmetric, turbulent, annular jets discharged through the nozzle of the SPP1980 SpraySyn burner under isothermal and reacting conditions, Experimental Thermal and Fluid Science 114 (2020) 110052. URL: https://doi.org/10.1016/j.expthermflusci.2020.110052. doi:10.1016/j.expthermflusci.2020.110052.

[42] A. J. Gröhn, S. E. Pratsinis, A. Sánchez-Ferrer, R. Mezzenga, K. Wegner, Scale-up of nanoparticle synthesis by flame spray pyrolysis: The high-temperature particle residence time, Industrial and Engineering Chemistry Research 53 (2014) 10734–10742. URL: https://pubs.acs.org/doi/10.1021/ie501709s. doi:10.1021/ie501709s.

[43] N. Jüngst, G. J. Smallwood, S. A. Kaiser, Visualization and image analysis of droplet puffing and micro-explosion in spray-flame synthesis of iron oxide nanoparticles, Experiments in Fluids 63 (2022) 60. URL: https://link.springer.com/10.1007/s00348-022-03411-y. doi:10.1007/s00348-022-03411-y.

[44] S. N. R. Inturi, T. Boningari, M. Suidan, P. G. Smirniotis, Visible-light-induced photodegradation of gas phase acetonitrile using aerosol-made transition metal (V, Cr, Fe, Co, Mn, Mo, Ni, Cu, Y, Ce, and Zr) doped TiO_2, Applied Catalysis B: Environmental 144 (2014) 333–342. doi:10.1016/j.apcatb.2013.07.032.

[45] C. Liu, S. Li, Y. Zong, Q. Yao, S. D. Tse, Laser-based investigation of the transition from droplets to nanoparticles in flame-assisted spray synthesis of functional nanoparticles, Proceedings of the Combustion Institute 36 (2017) 1109–1117. URL: https://linkinghub.elsevier.com/retrieve/pii/S1540748916302280. doi:10.1016/j.proci.2016.06.166.

[46] F. Pan, H. Lin, H. Zhai, Z. Miao, Y. Zhang, K. Xu, B. Guan, H. Huang, H. Zhang, Pd-doped TiO_2 film sensors prepared by premixed stagnation flames for CO and NH_3 gas sensing, Sensors and Actuators, B: Chemical 261 (2018) 451–459. URL: https://linkinghub.elsevier.com/retrieve/pii/S0925400518301898. doi:10.1016/j.snb.2018.01.173.

[47] H. Li, S. Pokhrel, M. Schowalter, A. Rosenauer, J. Kiefer, L. Mädler, The gas-phase formation of tin dioxide nanoparticles in single droplet combustion and flame spray pyrolysis, Combustion and Flame 215 (2020) 389–400. URL: https://linkinghub.elsevier.com/retrieve/pii/S0010218020300614. doi:10.1016/j.combustflame.2020.02.004.

[48] A. Witte, L. Mädler, Single droplet combustion of iron nitrate-based precursor solutions: Investigation of time- and size scales of isolated burning FSP-droplets, Applications in Energy and Combustion Science 14 (2023) 100147. URL: https://doi.org/10.1016/j.jaecs.2023.100147. doi:10.1016/j.jaecs.2023.100147.